Optics & Laser Technology 140 (2021) 107053

Contents lists available at ScienceDirect

Optics and Laser Technology

journal homepage: www.elsevier.com/locate/optlastec

Full length article

Mechanical properties and fracture behaviors in remote laser spot welding of quenching and partitioning 980 steel

Wei Zhang [a,b], Wu Tao [c], Shanglu Yang [c,d,*]

[a] Changchun Institute of Optics, Fine Mechanics and Physics, Chinese Academy of Sciences, Changchun, 130033, China
[b] University of Chinese Academy of Sciences, Beijing, 100049, China
[c] Shanghai Institute of Optics and Fine Mechanics, Chinese Academy of Sciences, Shanghai, 201800, China
[d] Center of Materials Science and Optoelectronics Engineering, University of Chinese Academy of Sciences, Beijing, 100049, China

ARTICLE INFO

Keywords:
Quenching and partitioning steel
Remote laser spot welding
Mechanical properties
Fracture behavior
Orientation imaging microscopy

ABSTRACT

Quenching and partitioning (Q&P) steel is one of most critical third generation steels in the automotive industry, which provides excellent mechanical properties and have a huge potential to significantly reduce vehicle weight and improve fuel efficiency. One of the bottlenecks for their applications in the automotive industry is the poor weldability. In this paper, a newly-developed remote laser spot welding (R-LSW) process was used to weld Q&P steel with laser beam moving along a spiral path. The welds with full penetration were obtained with laser power ranged between 2400 W and 3600 W, the weld morphology and mechanical properties of the joints were consistent, except for a little drop in case of 3600 W with the crater size of 0.65 mm. Under the shear tensile force, all the welds failed in partial thickness-partial pullout (PT-PP) mode, which was attributed to the formation of a large weld diameter. The weld failure process can be divided into four stages: (I) crack initiation; (II) crack propagation along the thickness and circumference of the joint; (III) crack propagation along the circumference of the joint; and (IV) instantaneous fracture. Furthermore, it was found that the coarse grain heat affected zone (CG-HAZ) has a lowest fraction of high-angle grain boundaries (HAGBs), resulting in the crack propagated along the CG-HAZ during stage II. During crack propagation, the fracture took place as a ductile fracture, but the instantaneous fracture occurred in quasi-cleavage characteristic.

1. Introduction

Advanced high strength steels (AHSSs) are increasingly applied in the automotive industry to reduce car body weight, improve fuel efficiency and collision safety. It is difficult for the first generation AHSSs, such as dual phase (DP) steels, and the second generation AHSSs, such as twinning induced plasticity (TWIP) steels, to achieve an appropriate balance between low cost and high strength [1]. Therefore, third generation AHSSs that have lower cost and the combination of high strength and ductility performance were proposed in order to achieve vehicle light weight goal [2]. Among the third generation steels, quenching and partitioning (Q&P) steel, considered as one of most popular third generation AHSSs, was firstly proposed by Speer et al. [3]. The microstructure of Q&P steel is composed of martensite, retained austenite and ferrite. The hard martensite ensures the strength of Q&P steel, the soft ferrite and residual austenite and the TRIP effect in the deformation process ensures the good plasticity of Q&P steel [4–6]. Q&P Steels are multiphase steels, which are prone to dynamic recovery, recrystallization, carbide precipitation, strain-induced transformation and other phenomena during welding process, resulting in multi-scale and multi morphology of joint microstructure [7–9]. Furthermore, the process window for welding Q&P steels is narrow, and the welding process is extremely sensitive, which is easy to produce a lot of expulsion [10].

Previous investigation on welding of Q&P steels mainly focused on the resistance spot welding (RSW). Wang et. al [11] investigated the fatigue behaviors and fracture modes of RSW Q&P980. It was indicated that the fatigue cracks initiated near the notch tip in HAZ, and then propagated through the weld thickness and base material. Liu et al. [12] found that phosphorus segregation played most important role in affecting the fracture mode of the joint, which led to the formation of liquation crack in the partial melting zone. Luo et al. [13] pointed out that compared with DP590 steel and 22MnB5 steel, Q&P980 steel had smaller grain misorientations, which led to more scatter strain distribution in the weld fusion zone.

* Corresponding author at: Shanghai Institute of Optics and Fine Mechanics, Chinese Academy of Sciences, Shanghai, 201800, China.
E-mail address: yangshanglu_lab@126.com (S. Yang).

https://doi.org/10.1016/j.optlastec.2021.107053
Received 1 December 2020; Received in revised form 8 February 2021; Accepted 2 March 2021
Available online 18 March 2021

Table 1
Chemical compositions and mechanical properties of Q&P980 steel.

C	Mn	Si	Al	S	P	Fe	YS/MPa	UTS/MPa	Elongation/%
0.190	2.270	1.730	0.030	0.001	0.011	Bal.	743	1108	18

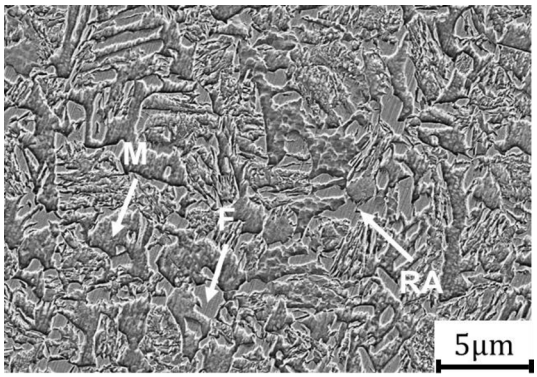

Fig. 1. Microstructure of Q&P980 steel (F: Ferrite; M: Martensite; RA: Retained Austenite).

Compared to resistance spot welding (RSW), laser welding is a single-side process and provides faster welding speed, lower distortion and high precision. The automotive industry always shows a strong interest in expanding laser welding application and replacing RSW with laser spot welding (LSW) [14]. Yang et al. [15] concluded that LSW had better reachability compared to RSW, thus providing better adaptability of configuration and spot arrangement. Zhang et al. [16] proposed a novel LSW method with real-time modulating laser focus position, which can improve the weld performance of Q&P980 joints. Furthermore, the novel LSW process can produce comparable weld nugget size and weld strength as RSW process. Compared to traditional LSW process, remote laser spot welding (R-LSW) is characterized by a larger distance between the laser focus lens and the workpiece [17] and provide more flexibility in designing laser beam path in various patterns such as a spiral path [18]. Spiral scanning welding is a method that laser is irradiated on work piece from one point and then scanned along a circle gradually being increased. Furthermore, the heat input into the molten pool can be dynamically adjusted by varying the process parameters. Moreover, the size of the molten pool can be increased as the diameter of the scanning circle increases, which can accommodate a larger assembly gap. Using laser spiral scanning can accommodate a larger assembly gap and provide a more stable welding process [19].

For the LSW joints, severer stress concentration at the weld edge was proved than that of RSW [20]. However, limited research on fracture behavior of LSW had been conducted. Obviously, high laser power increased the laser spot weld diameter and the coarse grain HAZ (CG-HAZ) experienced softening because of tempering, which had a counteractive influence on the tensile shear strength [21]. Alizadeh-Sh et al. [22] studied metallurgical and mechanical properties of circular laser spot weld in AISI 304 L steel. They claimed that the grain growth in heat affected zone (HAZ) led to its softening, and the mechanical properties of circular laser spot weld in AISI 304 L steel were mainly determined by fusion zone area and HAZ softening level. Tao et al.[23] proposed a mathematical solution for calculating the critical nugget diameter and predicting the failure mode based on failure mechanism and stress analysis of laser spot weld in mild steel. To sum up, it is lack of open literature about the fracture behavior and mechanism of LSW, especially for Q&P steel.

In this paper, a R-LSW process was used to join Q&P 980 steel under different laser power levels. Furthermore, various characteristics of typical welds were examined, including the microstructure, microhardness distribution, quasi-static performance and strain distribution of the weld. The crack propagation behavior and fracture mechanism were also elaborated.

2. Experimental setup

1.0 mm thick Q&P980 steel sheets produced by Baoshan Iron & Steel Co., Ltd. were used in this study. The nominal chemical compositions along with the typical yield strength (YS), ultimate tensile strength (UTS) and elongation are summarized in Table 1. The microstructure of Q&P980 base material consists of martensite, ferrite and retained austenite, as shown in Fig. 1.

Before carrying out R-LSW, the Q&P 980 metal sheet was cleaned with alcohol to avoid the influence of oil on welding and two sheets were clamped tightly to achieve a zero-gap joint. R-LSW was performed by an IPG YLS-10000 laser equipment integrated to a 6 axis ABB-IRB4600 robot. Laser beam was delivered to high-speed scanning galvanometer (Blackbird) using an optical fiber with core diameter of 150 μm. The laser beam was vertically delivered on the workpieces with a 0.56 mm beam diameter on focal position using a 460 mm focusing lens. A high-speed camera (Photron FASTCAM) was introduced to real time record the laser-induced plasma during LSW process. An illumination laser with 808 nm wavelength was applied for adjusting the contrast of the laser-induced plasma. And the frame was set at 2000 fps/s, the shutter speed is 1/1661538 s. The laser-induced plasma was captured in the parallel angle of the workpiece where the plasma located above top surface and below bottom surface can be observed. Schematic diagram of the experimental system was depicted in Fig. 2a. The laser beam path

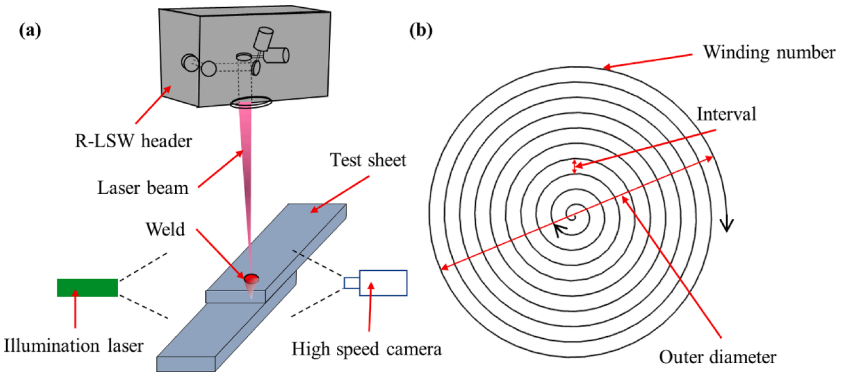

Fig. 2. Schematic of R-LSW process: (a) experimental setup; (b) spiral laser beam path.

Table 2
R-LSW parameters used in this study.

Laser power (W)	Velocity (m/min)	Outer diameter (mm)	Winding number	Interval (mm)	Total welding time (s)
2400–3600	10	7	12	0.292	0.793

is an equidistant spiral weld, and the welding direction is from inside to outside, as shown in Fig. 2b. Specific details of welding parameters are presented in Table 2. The laser power increased from 2400 W to 3600 W with an interval of 200 W.

The cross-sectioned welds were prepared by standard process of electrical wire cutting, mounting and mechanical polishing. And polished samples were etched by 4% nital reagents. Optical microscopy (OM, KEYENCE VHX-6000) and scanning electron microscopy (SEM, ZEISS Sigma 500) were used to examine the detailed microstructure of the welds. The microhardness tests were carried out for a dwell time of 10 s with an applied load of 300 g at an interval of 0.15 mm. For misorientation angle distribution analysis, the samples were polished using silica solution of 0.05 μm for 20 min. And the characterization was made by electron back scatter diffraction (EBSD, OXFORD Symmetry) measurement with the step size of 0.10 μm. Besides, the data was post analyzed by software of AZtecCrystal.

The quasi static tensile shear test was performed at room temperature with the cross-head speed of 3 mm/min by a mechanical tester (SUNS Co., Ltd.) according to ISO 14323-2015, as shown in Fig. 3a. And a high-speed camera (Photron FASTCAM) was introduced to real time record the fracture behaviors of crack propagation during tensile shear test. A digital image correlation (DIC) system was also applied to study the strain distribution. The steel sheets were cut into 105 mm × 45 mm coupons and then joined with an overlap of 35 mm, as shown in Fig. 3b. Three replicas were performed for each laser power condition.

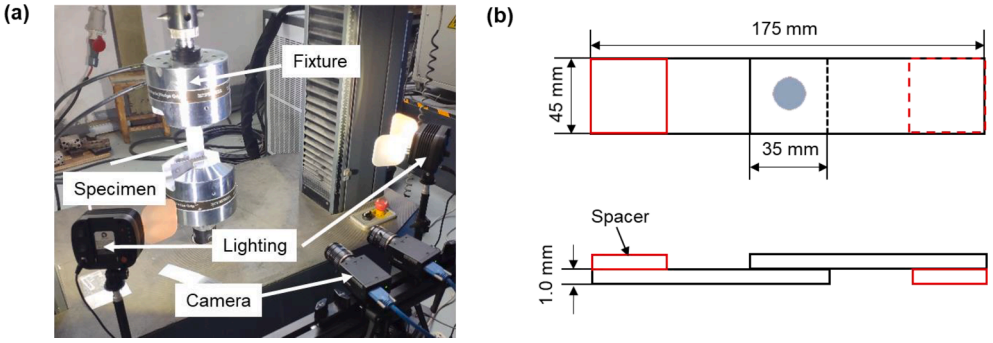

Fig. 3. (a) Experimental setup of tensile-shear test; (b) schematic illustration of tensile-shear specimen.

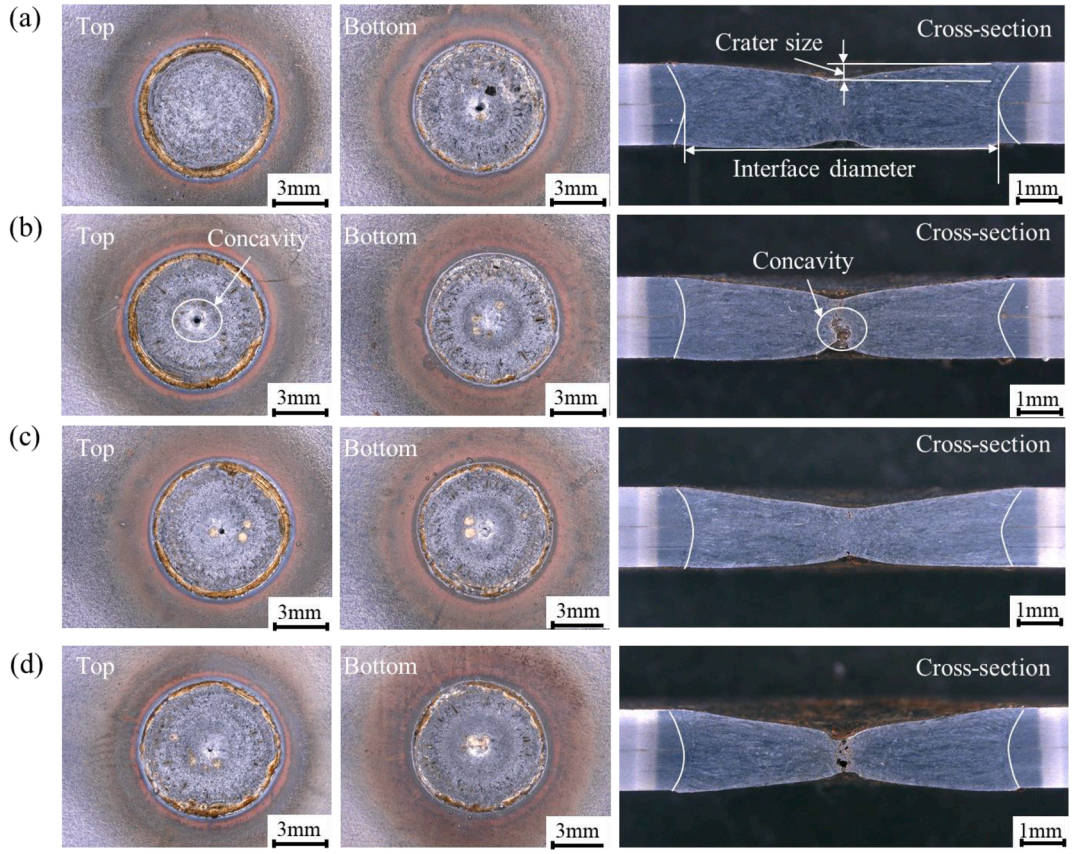

Fig. 4. Morphology of remote laser spot welds with different laser powers: (a) 2400 W; (b) 2800 W; (c) 3200 W; (d) 3600 W.

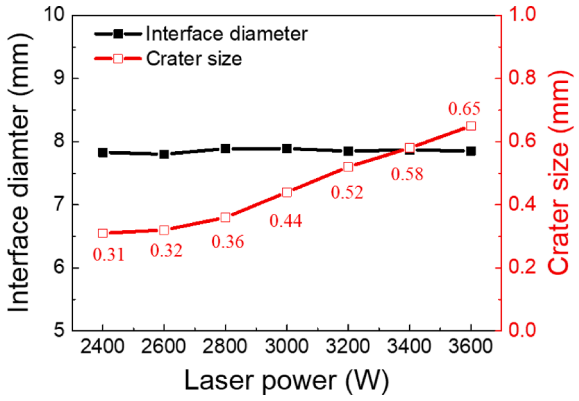

Fig. 5. Relationship between the interface diameter and crater size with different laser power.

3. Results and discussion

3.1. Effect of laser power on the weld morphology and plasma behavior

Effect of laser power on the weld morphology was firstly investigated. Under the condition that other welding parameters remain unchanged, the laser power determined the heat input of R-LSW weld. Fig. 4 shows the top, bottom and cross-section views of the typical welds, which were obtained with different laser power. As shown, the cross-sections of all welds had "X" shape. In addition, concavity in the weld center was observed due to the shrinkage during the solidification process and many materials lost during laser welding process. It can be concluded from the Fig. 4 that the crater size increased with the increasing laser power.

Fig. 5 shows the effect of laser power on the interface diameter and crater size. As shown, the interface diameter of the weld did not change significantly as the laser power changed from 2400 W to 3600 W, however, the crater size increased from 0.31 mm to 0.65 mm. The deep crater formation in the weld center was caused by the strong effect of recoil pressure resulted from the intensive laser beam energy intensity. The higher laser power is, the higher recoil is, causing ejection of large amounts of liquid metal from the molten pool because of the failure of the surface tension to balance it. And this phenomenon related to the absorption of laser energy by welds.

In order to study the difference of laser energy absorption with different laser power, a high-speed camera was used to real-time monitor the dynamic behaviors of laser-induced plasma and plume from the beginning to the end of R-LSW process, which the total welding time was 0.793 s. According to different brightness values, the number of pixels of laser-induced plasma and plume over time were extracted by Matlab software as shown in Fig. 6. Besides, the plasma area is proportional to the number of pixels. It can be concluded from Fig. 6 that the plasma area above the top surface and below the bottom surface were different with different laser power. All welding parameters were

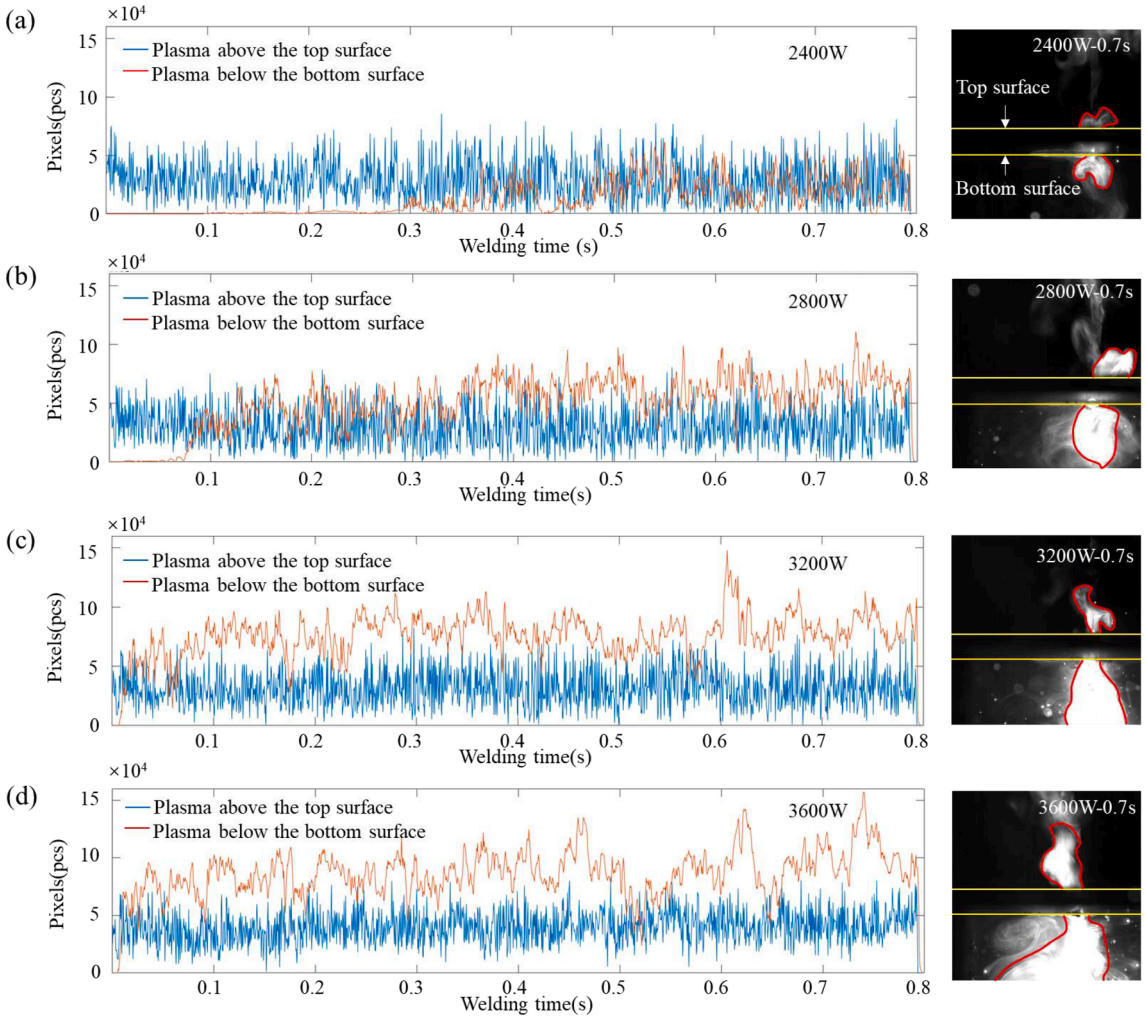

Fig.6. The varying pixels of laser-induced plasma and plume with different laser power: (a) 2400 W; (b) 2800 W; (c) 3200 W; (d) 3600 W.

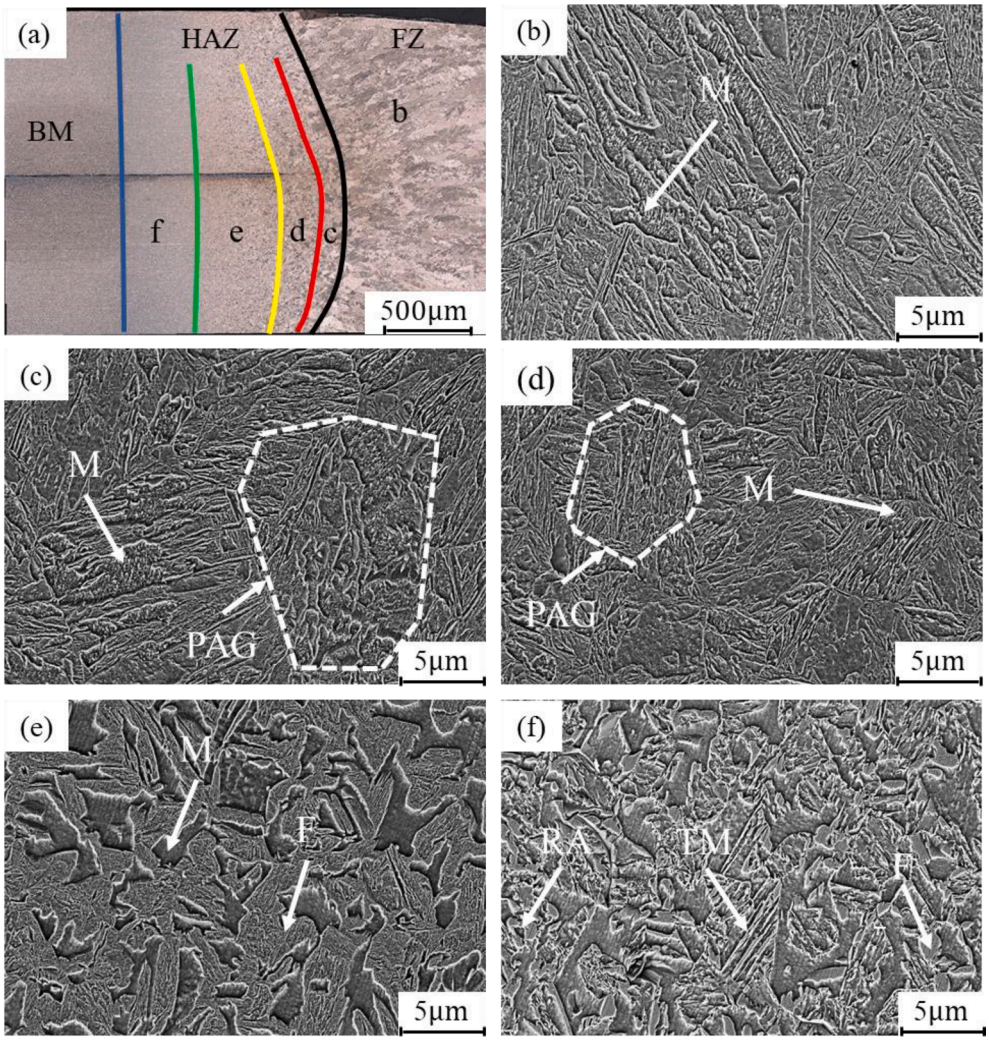

Fig. 7. The microstructures of different regions of R-LSW joint: (a) an overall view of etched sample where the microstructures in areas of (b–f) are indicated; (b) fusion zone (FZ); (c) coarse grain HAZ (CG-HAZ); (d) fine grain HAZ (FG-HAZ); (e) intercritical HAZ (IC-HAZ); (f) subcritical HAZ (SC-HAZ). (laser power of 3000 W).

kept constant except for the laser power ranging from 2400 W to 3600 W with an increment of 400 W. During R-LSW process, a portion of laser energy is scattered, refracted and absorbed and the remnant portion is absorbed by the workpiece to effect on the molten pool and enlarge it. When the welding time was 0.3 s with laser power of 2400 W in Fig. 6a, the plasma appeared below the bottom surface. This phenomenon showed that the laser has fully penetrated the bottom plate. When the size of plasma and plume below the bottom sheet is larger than that above the top sheet, it suggested that most of laser beam energy is lost from the bottom sheet and only little portion is absorbed by the molten pool, which leads to the formation of a small weld size [16]. As shown in Fig. 6, the plasma area of bottom surface was smaller than that of the top surface as the increase in the welding time. This phenomenon showed that the laser was basically absorbed by the molten pool, resulting in a good quality weld and small crater size. When the welding time was 0.4 s with laser power of 2800 W, the laser-induced plasma and plume below the bottom surface had a larger size than that above the top surface of two metal sheets as shown in Fig. 6b. This phenomenon indicated that part of laser beam energy was lost, resulting in a larger crater size. Furthermore, it can be seen in Fig. 6c and d, with the increase of laser power to 3200 W and 3600 W, the plasma area of the bottom surface became larger than 2800 W. And the pixels of plasma below the bottom surface of 3600 W was 8.63×10^4pcs, which was bigger than that of 7.58×10^4pcs with 3200 W. This phemomena indicated that most of laser beam energy was lost when laser power was 3600 W, resulting in a larger crater size.

3.2. Microstructure and hardness

Fig. 7 and Fig. 8 show the microstructures and microhardness profiles at different regions of weld with laser power is 3000 W. It can be seen in the Fig. 7b that columnar crystal martensite was observed in the fusion zone (FZ), with an average hardness value of 496HV, as shown in Fig. 8. The thermal cycle in various areas of heat affected zones (HAZ) is different due to laser beam travelling with varying distance away from the weld center, which leads to different temperature distribution. As a result, cooling velocity to room temperature is different, thus producing various microstructures in HAZ. The heat affected zone is subdivided into four zones: (a) coarse grain heat affected zone (CG-HAZ); (b) fine grain heat affected zone (FG-HAZ); (c) intercritical heat affected zone (IC-HAZ) and (d) subcritical heat affected zone (SC-HAZ). And the CG-HAZ is the heat affected zone near the fusion zone, corresponding to the C zone in Fig. 7a. The temperature of CG-HAZ was much higher than Ac3 and the residence time of high temperature was longer. The original austenite grains will undergo significant growth and becomes coarse martensite. Prior austenite grain (PAG) boundaries are shown in Fig. 7c. The hardness of CG-HAZ is similar with FZ (~496 HV), which is due to the formation of lath martensite. In addition, the temperature of FG-HAZ also exceeded Ac3, but the growth of PAG was restricted due to the short residence time at high temperature. Therefore, fine and uniform

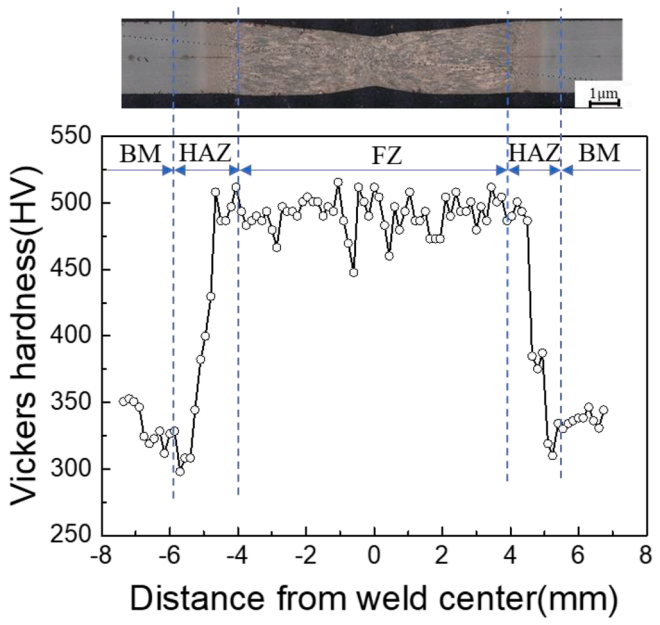

Fig. 8. Microhardness profiles of the joints obtained with laser power was 3000 W.

martensite with highest hardness (at a value of ~520 HV) was formed under rapid cooling condition in Fig. 7d. The peak temperature of IC-HAZ lies between Ac1 and Ac3, resulting in an incomplete austenitization. Therefore, the microstructure in IC-HAZ contains ferrite and martensite in Fig. 7e. Furthermore, due to the increased distance from the fusion zone, the volume fraction of martensite decreased, resulting in the hardness of IC-HAZ dropped from 496HV to 430HV. The SC-HAZ temperature is lower than the Ac1 line, which make partial pre-existing martensite in the FZ to be decomposed into tempered martensite (TM), as shown in Fig. 7f. In addition, a softening zone appeared in SC-HAZ due to the tempering of martensite compared with microstructure in FZ [8], and the hardness value decreased to 310HV.

3.3. Effect of laser power on the mechanical properties

The relationship between peak load and extension of the welds and different laser power were shown in Fig. 9. When the laser power increased from 2400 W to 3400 W, the peak load and extension of the welds were remained about 22.00 kN and 1.21 mm, respectively, as shown in Fig. 9a. When the laser power increased to 3600 W, the peak load decreased to 21.31kN and the extension decreased to 1.12 mm. This suggests that the appropriate laser power for R-LSW welding of 1.0 mm thick Q&P980 steel was between 2400 W and 3400 W. It can be clearly seen in Fig. 9b that when the laser power was 2400 W to 3400 W, the mechanical properties of the joints were stable and the load-displacement curves were basically consistent. However, when the laser power was 3600 W, the mechanical properties decreased obviously. The reason of the deteriorated mechanical properties is because of the formation of a large crater in the weld center under high laser power effect [24].

In order to study the fracture behavior of welds under the stable mechanical properties, the welding joints with laser power of 2400 W, 3000 W and 3400 W were researched. Fig. 10 shows the fracture morphology of R-LSW Q&P980 weld after tensile shear tests. As shown, all the welds fractured with partial thickness-partial pullout failure (PT-PP) mode, in which part of the mating sheet thickness was removed, and fastigiate crack propagated to the fusion zone during the separation process [10]. The process of PT-PP failure mode can be divided into two locations of I and II, as shown in Fig. 10b, e and h. The fracture route of location I was along the boundary of coarse grain heat affected zone (CG-HAZ), as can be seen in Fig. 10c, f and i, and the fracture route of location II was along the fusion zone at a certain angle with the tensile load. Since the fracture mode and location of joints with laser power of 2400 W, 3000 W and 3400 W were similar, the joint with laser power of 3000 W was analyzed in detail to analyze the fracture behavior.

3.4. The fracture behavior of typical weld

DIC system was applied to real-time record the strain distribution variation during tensile shear testing. Fig. 11 shows the side-view images recorded by DIC to reflect major strain distribution, in which the white dotted circle in the figure is the weld boundary. Three moments that joint undergone the tensile shear test were chosen for the comparisons. As shown, the base material experienced strain and work hardening at the beginning of the tensile test, refer to Fig. 11b. Furthermore, at the moment with the displacement of 1.20 mm, the strain was concentrated on the edge of weld, as indicated in Fig. 11c, which indicated that the elliptical area of weld began to fracture.

To clearly understand the weld crack initiation mechanism, the tensile shear tests were intentionally interrupted at the displacement of 0.40 mm, 0.80 mm and 1.20 mm just before the weld failure took place in the test coupons, respectively. Fig. 12 was the cross-section observation of different fractured welds with various tensile displacements. It can be seen from Fig. 12a and b that the crack did not start and propagate toward the FZ at the displacement of 0.4 mm and 0.8 mm, respectively. When the tensile displacement was 1.20 mm, a slight crack took place which was perpendicular to the direction of tensile force. It can be concluded from this phenomenon that crack initiated at the CG-HAZ when weld fractured instantly.

In order to study dynamic behaviors of crack path, a high speed camera was used to real-time monitor the fracture process. Fig. 13 shows the load–displacement curve and top view images of the weld fracture

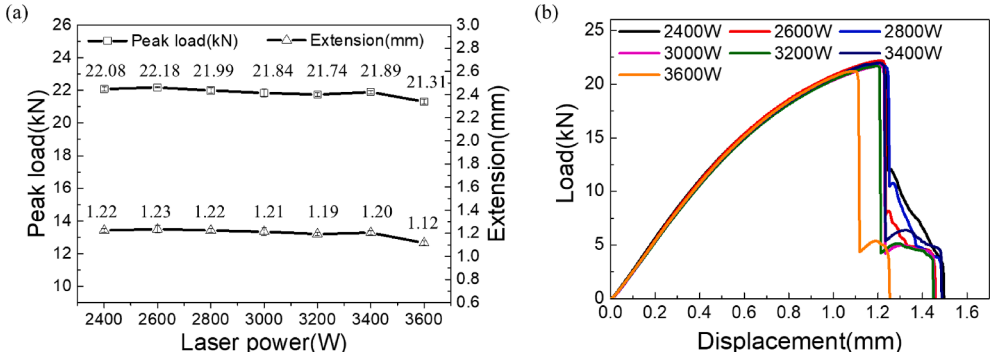

Fig. 9. Effect of laser power on the mechanical properties: (a) relationship of peak load and extension with laser power; (b) load-displacement curves of the joints obtained with laser power from 2400 W to 3600 W.

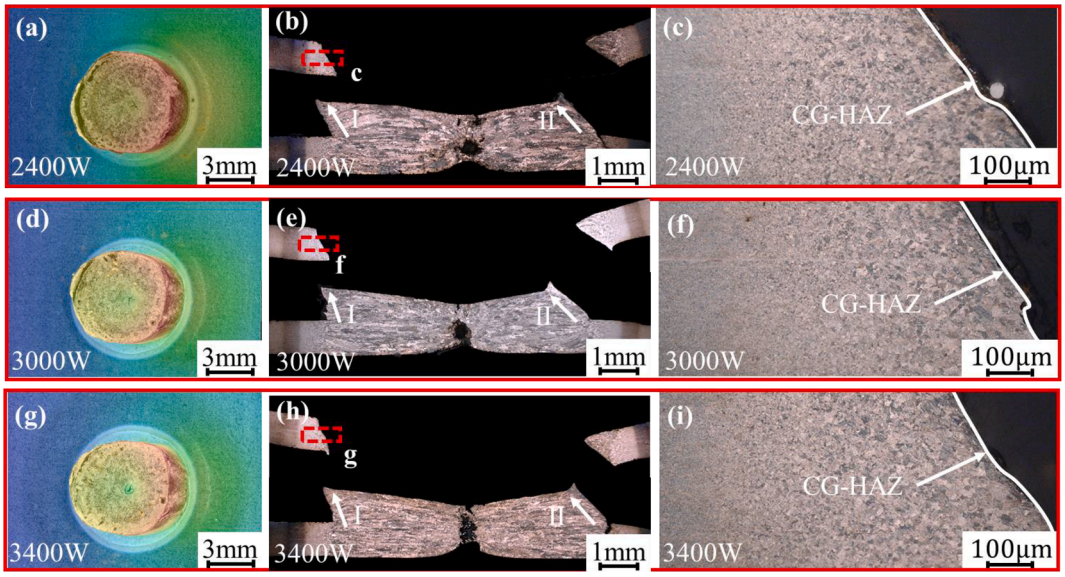

Fig. 10. Typical partial thickness-partial pullout failure fracture mode of remote laser spot weld in Q&P980 steel: (a), (d) and (g) fracture surface of 2400 W, 3000 W and 3400 W; (b), (e) and (h) fracture cross-section of 2400 W, 3000 W and 3400 W; (c), (f) and (i) fracture location of 2400 W, 3000 W and 3400 W.

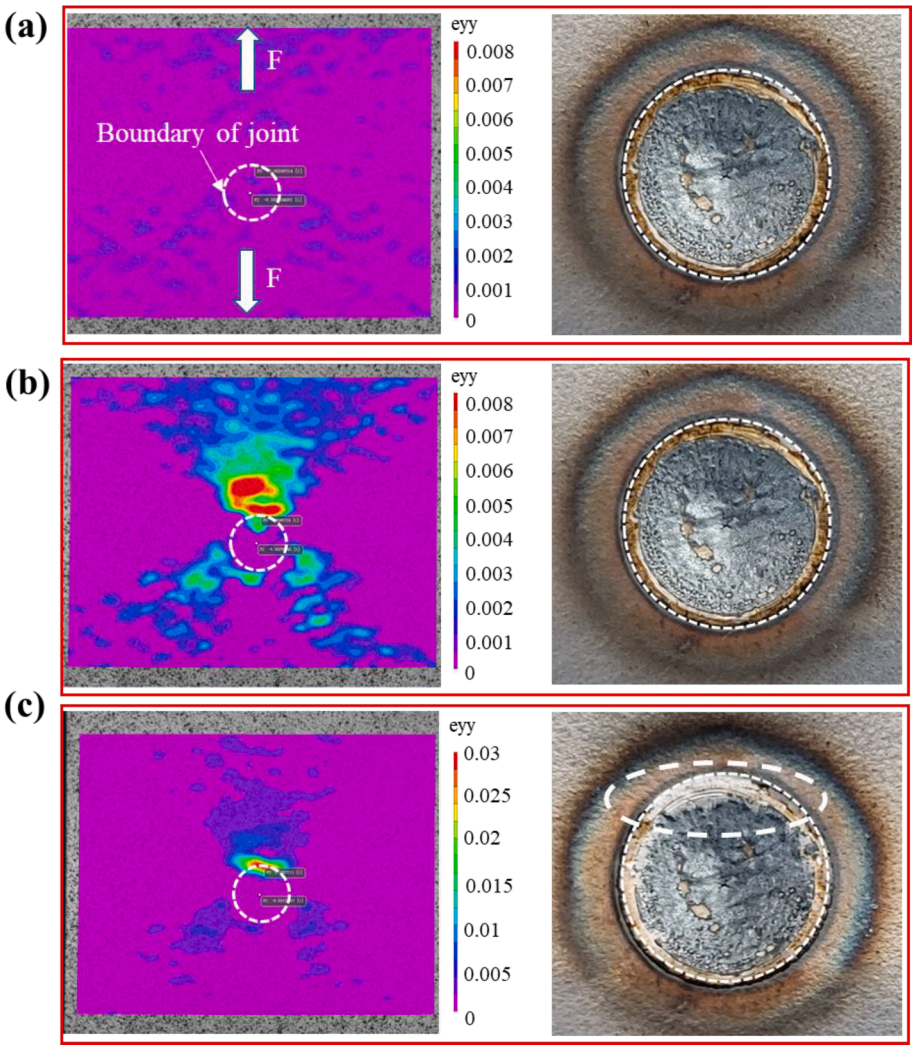

Fig. 11. Strain distribution on top sides at different time during tensile shear test of laser weld achieved at the power of 3000 W: (a) At initial moment with the displacement of 0 mm; (b) At displacement of 1.00 mm; (c) At displacement of 1.20 mm with the maximum load.

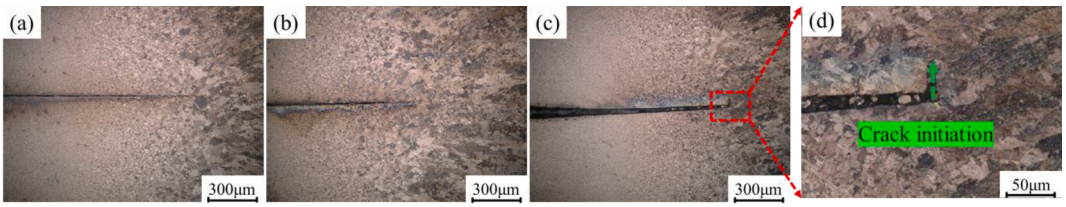

Fig. 12. Cross-sectional views of the weld under different displacements with laser power of 3000 W: (a) 0.40 mm displacement; (b) 0.80 mm displacement; (c) 1.20 mm displacement; (d) crack initiation under displacement is 1.20 mm.

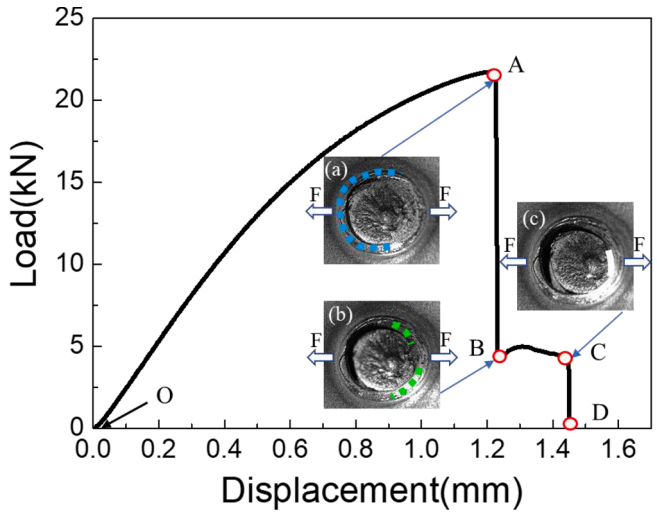

Fig. 13. The load-displacement curve and top view images of the fracture process obtained by high-speed camera: (a) point A with the displacement of 1.21 mm; (b) point B with the displacement of 1.22 mm; (c) point C with the displacement of 1.45 mm. (laser power of 3000 W).

process by high-speed camera. And schematic diagrams of different fracture stages were presented in Fig. 14. The crack started to initiate when the peak load reached the maximum at point A. Then the tensile load suddenly decreased as the tensile shear test continued. This phenomenon indicated that point A was the beginning of the internal fracture route, as seen in Fig. 14a. At the moment of fracture stage AB, Fig. 13a shows the crack initiated from the notch between the two plates, and then expanded to half of the joint along the circumferential direction, which was indicated by the blue dotted line in the figure. Besides, during stage AB, the crack propagated along the boundary between the CG-HAZ which represented the joint broken its strength limit as shown in Fig. 14b. And this stage is a most important process in the mechanical property analysis of joint because the joint is destroyed instantly. With the increase of the displacement, the downward trend of the curve becomes slower during stage BC, the crack continued to propagate along the circumference of the joint, as shown by the green dotted line in Fig. 13b and Fig. 14c. When the displacement kept increasing, the deflection angle of the two plates increased, resulting in the two plates were completely separated due to the joint cannot bear the shear force, as indicated by the white line in Fig. 13c. Besides the crack propagates along the boundary of the joint which was displayed in Fig. 14d.

It was concluded that, the PT-PP fracture process included four stages, which were crack initiation stage (OA), crack propagation stage along the thickness direction and circumference of the joint (AB), crack propagation stage along the circumference of the joint (BC) and instantaneous fracture stage (CD).

Typical fracture surface of typical R-LSW joint obtained by laser power of 3000 W was shown in Fig. 15. Fig. 15a shows overall view of the fractured joint and Fig. 15b–d are SEM images of fracture surface of zones b-d, which correspond to fracture location I and fracture location II in Fig. 8. As shown in Fig. 15b, many small dimples alternate with each other, which shows ductile fracture characteristic. Furthermore, larger size dimples and cleavage fracture were observed in area c and the depth of dimples with large size also decreased significantly, as shown in Fig. 15c. These shallow dimples confirmed that the joint ductility was reduced. Also, it was shown in Fig. 15d that both large area of river-like pattern and dimples were observed in zone d, indicating a quasi-cleavage characteristic.

3.5. *Effect of orientation angle of grain boundary on fracture mechanism*

As known, the temperature distribution in different areas of the joint would greatly affect the cooling rate, which ultimately has a direct influence on the fraction of high angle grain boundary (HAGB) [25]. HAGB is beneficial to deflect or even arrest the propagation of cracks, thus enhancing the impact toughness [26]. Fig. 16 shows the inverse pole figure (IPF) of fracture location I corresponds to crack propagation (AB), and Fig. 17 shows the orientation image maps (OIMs) to achieve more detailed information concerning the heterogeneity and crystallographic features of the welded joint. As analyzed above, the microstructure in the FZ was largely consisted of elongated martensite, which can be confirmed further by Fig. 17a. The different regions of the joint were composed of high angle grain boundaries (HAGBs) and low angle grain boundaries (LAGBs). Normalized frequency of HAGBs (misorientation $\theta > 10^\circ$) of the FZ is 49.0%, while that of LAGBs (misorientation $\theta < 10^\circ$) is 51.0%, as shown in Fig. 17a. It was indicated that the CGHAZ (Fig. 17b) showed a typical structure of isometric crystal. Comparing the grain boundary maps with FZ (Fig. 17a), it was found that CGHAZ had fewer substructures with a lower frequency (36.8%) of HAGBs and a higher frequency (63.2%) of LAGBs. As the distance increased from the CGHAZ to ICHAZ, the grains gradually became finer, and the proportion of HAGBs gradually increased. The BM has a grain boundary misorientation distribution of HAGBs (64.5%) and LAGBs (35.5%), as shown in Fig. 17f.

The grain boundary energy increased with the increase of the grain boundary orientation angle. The HAGBs which have the misorientation $>10^\circ$ mainly makes crack difficult to be propagated, thereby improving the toughness of the joint. At the region of LAGBs, the crack is more sensitive to propagate, and it can propagate along the next grain boundary and the toughness decreases [27]. During the tensile shear test, the crack overcomes and consumes more energy to expand in the high angle grain boundary, which effectively slows the expansion of the crack to a certain extent. During the tensile process, the crack tended to propagate to the FZ after initiation. Since the CG-HAZ has the lowest high-angle grain boundaries, the crack initiated at the CG-HAZ.

In order to analyze fracture route, the distribution of high-angle grain boundaries in the entire area corresponding to the Fig. 16 need to be obtained. The area was divided into a lattice composed of 50 μm × 40 μm boxes. By measuring the proportion of HAGBs in each box, the MATLAB software was used to obtain a cloud diagram of the HAGBs ratio of the entire area. As shown in Fig. 18, different colors indicate different fraction of HAGBs. The white line in the figure shows the position where the proportion of the HAGBs' propagation is small. It was suggested that in this area, the fraction of high-angle grains is less than

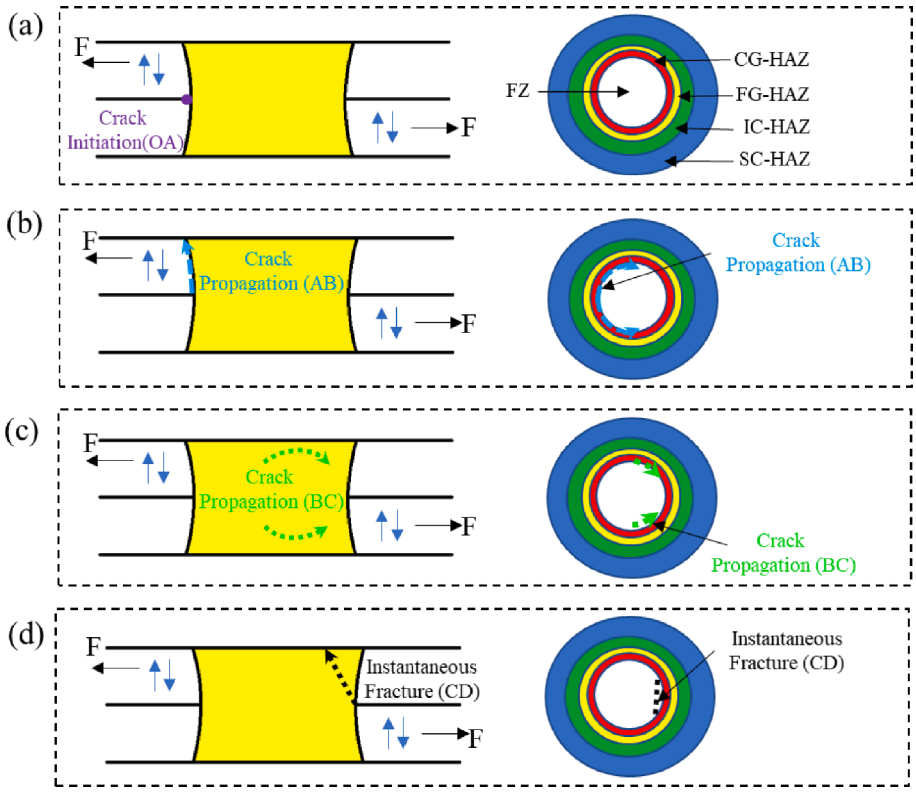

Fig. 14. Schematic diagrams of different fracture stages: (a) cross-section and top surface of the crack initiation (OA); (b) cross-section and top surface of crack propagation (AB); (c) cross-section and top surface of crack propagation (BC) (d) cross-section and top surface of instantaneous fracture (CD).

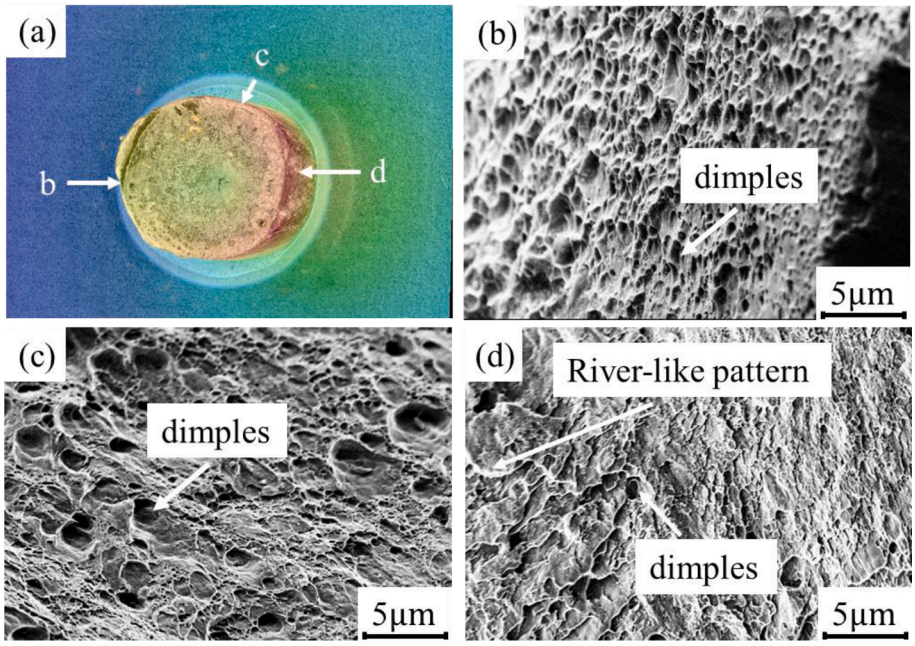

Fig. 15. Top view and SEM micrographs of fracture surface of R-LSW joint: (a) top view of fractured weld; (b)-(d) SEM images of the fractured surface located at zones of b-d. (laser power of 3000 W).

low-angle grains, and crack tended to propagate along this line. Besides, the white line in the cloud diagram was shown in the IPF map. It can be concluded that the place with the lowest proportion of high-angle grain boundaries was at the CGHAZ, which caused the fracture to expand along this path.

4. Conclusions

In this study, a newly remote laser spot welding process is developed and the effect of various laser power on the morphology, plasma behavior and mechanical properties of the welds are studied. Furthermore, the fracture process and mechanism of the weld during the tensile

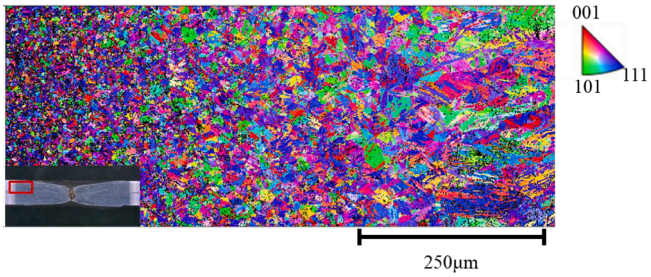

Fig. 16. Inverse pole figure (IPF) of crack propagation (AB) region.

shear testing are analyzed. The main conclusions can be drawn as follows:

1. The larger crater size with higher laser power is attributed to the welds failing to fully absorb the laser energy. When the crater size is less than 0.58 mm of R-LSW welds with laser power range between 2400 W and 3400 W, the morphology of the welds are stable and the mechanical properties are consistent.
2. The welds all fail in partial thickness-partial pullout fracture (PT-PP) under the tensile shear load. And the fracture process can be divided into four stages: (I) crack initiation; (II) crack propagation along the thickness and the circumference of the joint; (III) crack propagation along the circumference of the joint; and (IV) instantaneous fracture.

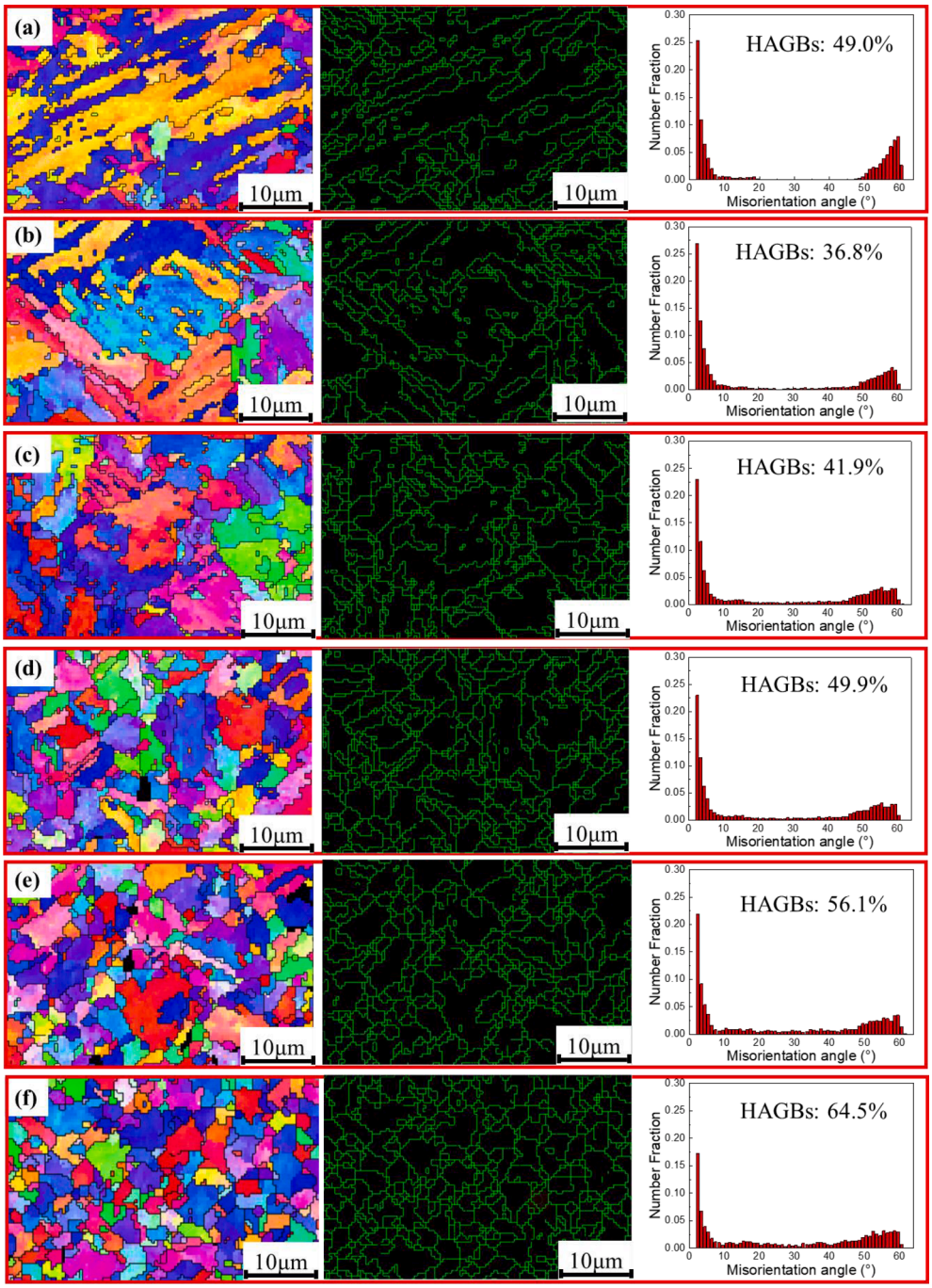

Fig. 17. Inverse pole figures (IPFs), grain boundary maps and fraction of high angle grain boundaries (HAGBs) of the weld analyzed by EBSD: (a) FZ, (b) CG-HAZ, (c) FG-HAZ, (d) SC-HAZ, (e) IC-HAZ and (f) BM. (Green lines indicate grain boundaries with a misorientation angle higher than 10°).

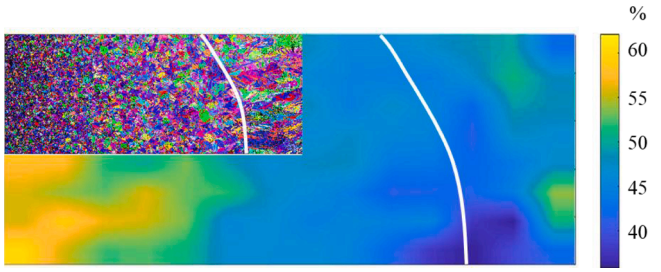

Fig. 18. The fraction of HAGBs and IPF map of the weld (laser power of 3000 W).

The peak load of joint occurs in stage II according to the analysis of fracture process.

3. During tensile shear testing, the strain concentration is switched from the base material to the periphery of the joint immediately when the applied tensile load is maximum.
4. The CG-HAZ contains a small fraction of high angle grain boundaries, which plays a role of easy path for crack propagation. When the tensile shear load is applied, the crack propagates along the CG-HAZ zone at the stage II of tensile shear test.

CRediT authorship contribution statement

Wei Zhang: Conceptualization, Visualization, Writing - original draft, Validation. **Wu Tao:** Writing - review & editing, Validation, Supervision. **Shanglu Yang:** Writing - review & editing, Funding acquisition, Project administration, Supervision.

Declaration of Competing Interest

The authors declare that they have no known competing financial interests or personal relationships that could have appeared to influence the work reported in this paper.

Acknowledgement

This work was supported by the Chinese Academy of Sciences [grant number 292017312D1100301]; Shanghai Municipal Economic and Informatization Commission [grant number GYQJ-2019-1-33];

References

[1] M.G. Lee, S.J. Kim, H.N. Han, W.C. Jeong, Application of hot press forming process to manufacture an automotive part and its finite element analysis considering phase transformation plasticity, Int. J. Mech. Sci. 51 (2009) 888–898, https://doi.org/10.1016/j.ijmecsci.2009.09.030.

[2] W. Cao, C. Wang, C. Wang, J. Shi, M. Wang, H. Dong, Y. Weng, Microstructures and mechanical properties of the third generation automobile steels fabricated by ART-annealing, Sci. China Technul Sc 55 (2012) 1814–1822, https://doi.org/10.1007/s11431-012-4877-7.

[3] J. Speer, D.K. Matlock, B.C. De Cooman, J.G. Schroth, Carbon partitioning into austenite after martensite transformation, Acta Mater. 51 (2003) 2611–2622, https://doi.org/10.1016/s1359-6454(03)00059-4.

[4] Y. Wang, K. Zhang, Z.H. Guo, N.L. Chen, Y.H. Rong, A new effect of retained austenite on ductility enhancement in high strength bainitic steel, Mater. Sci. Eng. A-Struct. Mater. Properties Microstruct. Process. 552 (2012) 288–294, https://doi.org/10.1016/j.msea.2012.05.042.

[5] S. Yan, X. Liu, W.J. Liu, T. Liang, B. Zhang, L. Liu, Y. Zhao, Comparative study on microstructure and mechanical properties of a C-Mn-Si steel treated by quenching and partitioning (Q&P) processes after a full and intercritical austenitization, Mater. Sci. Eng. A-Struct 684 (2017) 261–269, https://doi.org/10.1016/j.msea.2016.12.026.

[6] J. Sun, H. Yu, Microstructure development and mechanical properties of quenching and partitioning (Q&P) steel and an incorporation of hot-dipping galvanization during Q&P process, Mater. Sci. Eng. A-Struct. 586 (2013) 100–107, https://doi.org/10.1016/j.msea.2013.08.021.

[7] Z. Li, R. Kiran, J. Hu, L.G. Hector, A.F. Bower, Analysis and design of a three-phase TRIP steel microstructure for enhanced fracture resistance, Int. J. Fract. 221 (2020) 53–85, https://doi.org/10.1007/s10704-019-00405-6.

[8] W. Guo, Z. Wan, P. Peng, Q. Jia, G. Zou, Y. Peng, Microstructure and mechanical properties of fiber laser welded QP980 steel, J. Mater. Process Tech. 256 (2018) 229–238, https://doi.org/10.1016/j.jmatprotec.2018.02.015.

[9] Z.W. Wang, H. Zhang, X.H. An, L.H. Wu, P. Xue, Q.C. Zhang, D.R. Ni, B.L. Xiao, Z. Y. Ma, Achieving equal strength joint to parent metal in a friction stir welded ultra-high strength quenching and partitioning steel, Mater. Sci. Eng. A-Struct. 793 (2020), https://doi.org/10.1016/j.msea.2020.139979.

[10] M. Pouranvari, S.P.H. Marashi, Critical review of automotive steels spot welding: process, structure and properties, Sci. Technol. Weld. Joi 18 (2013) 361–403, https://doi.org/10.1179/1362171813y.0000000120.

[11] B. Wang, Q.Q. Duan, G. Yao, J.C. Pang, X.W. Li, L. Wang, Z.F. Zhang, Investigation on fatigue fracture behaviors of spot welded Q&P980 steel, Int. J. Fatigue 66 (2014) 20–28, https://doi.org/10.1016/j.ijfatigue.2014.03.004.

[12] X.D. Liu, Y.B. Xu, R.D.K. Misra, F. Peng, Y. Wang, Y.B. Du, Mechanical properties in double pulse resistance spot welding of Q&P 980 steel, J. Mater. Process Tech. 263 (2019) 186–197, https://doi.org/10.1016/j.jmatprotec.2018.08.018.

[13] C. Luo, Y. Zhang, Constitutive relationship of fusion zone in the spot welds of advance high strength steels, J. Manuf. Process 45 (2019) 624–633, https://doi.org/10.1016/j.jmapro.2019.08.007.

[14] F. Dorsch, M. Dahmen, Laser beam welding of new ultra-high strength and supra-ductile steels, in: HIGH-Power Laser Materials Processing: Lasers, Beam Delivery, Diagnostics, and Applications IV (2015). https://doi.org/10.1117/12.2084701.

[15] Y.S. Yang, S.H. Lee, A study on the joining strength of laser spot welding for automotive applications, J. Mater. Process Tech. 94 (1999) 151–156, https://doi.org/10.1016/s0924-0136(99)00094-1.

[16] W. Zhang, S. Yang, Z. Lin, W. Tao, Weld morphology and mechanical properties in laser spot welding of quenching and partitioning 980 steel, J Manuf. Process 56 (2020) 1136–1145, https://doi.org/10.1016/j.jmapro.2020.05.057.

[17] M.F. Zaeh, J. Moesl, J. Musiol, F. Oefele, Material processing with remote technology - revolution or evolution? Laser Assist Net Shape Eng. 6, Proc. Lane 2010 5 (2010) 19–33, https://doi.org/10.1016/j.phpro.2010.08.119. Part 1.

[18] W.T. David Yang, Paolo A. Novelletto, Yu Pan, Justin Wolsker, Remote laser welding of overlapping metal workpieces using helical path(s) (2020).

[19] J.B. Wang, T. Nakagawa, Y. Mukai, H. Nishimura, M. Ryudo, A. Kawamoto, Development of laser processing robot integrated system solution (LAPRISS) for remote laser welding, robotic welding, intelligence and automation, Rwia'2014 363 (2015) 119–131, https://doi.org/10.1007/978-3-319-18997-0_10.

[20] W. Tao, L.Q. Li, Y.B. Chen, L. Wu, Joint strength and failure mechanism of laser spot weld of mild steel sheets under lap shear loading, Sci. Technol. Weld Joi 13 (2013) 754–759, https://doi.org/10.1179/136217108x338917.

[21] J. Kundu, T. Ray, A. Kundu, M. Shome, Effect of the laser power on the mechanical performance of the laser spot welds in dual phase steels, J. Mater. Process Tech. 267 (2019) 114–123, https://doi.org/10.1016/j.jmatprotec.2018.12.014.

[22] M. Alizadeh-Sh, F. Falsafi, M. Masoumi, S.P.H. Marashi, M. Pouranvari, Laser spot welding of AISI 304L: metallurgical and mechanical properties, Ironmak. Steelmak. 41 (2014) 161–165, https://doi.org/10.1179/1743281213y.0000000112.

[23] W. Tao, L.Q. Li, Y.B. Chen, L. Wu, Joint strength and failure mechanism of laser spot weld of mild steel sheets under lap shear loading, Sci. Technol. Weld Joi 13 (2008) 754–759, https://doi.org/10.1179/136217108x338917.

[24] M.A. Ezazi, F. Yusof, A.A.D. Sarhan, M.H.A. Shukor, M. Fadzil, Employment of fiber laser technology to weld austenitic stainless steel 304 l with aluminum alloy 5083 using pre-placed activating flux, Mater. Design 87 (2015) 105–123, https://doi.org/10.1016/j.matdes.2015.08.014.

[25] Y. You, C. Shang, N. Wenjin, S. Subramanian, Investigation on the microstructure and toughness of coarse grained heat affected zone in X-100 multi-phase pipeline steel with high Nb content, Mater. Sci. Eng. A-Struct. 558 (2012) 692–701, https://doi.org/10.1016/j.msea.2012.08.077.

[26] A. Lambert-Perlade, A.F. Gourgues, A. Pineau, Austenite to bainite phase transformation in the heat-affected zone of a high strength low alloy steel, Acta Mater. 52 (2004) 2337–2348, https://doi.org/10.1016/j.actamat.2004.01.025.

[27] Y. Shen, J. Leng, C. Wang, On the heterogeneous microstructure development in the welded joint of 12MnNiVR pressure vessel steel subjected to high heat input electrogas welding, J. Mater. Sci. Technol. 35 (2019) 1747–1752, https://doi.org/10.1016/j.jmst.2019.03.035.